Low Temperature Physics/Fizika Nizkikh Temperatur, 2014, v. 40, No. 3, pp. 250–258

Current–voltage characteristics of Nb–carbon–Nb junctions

I.P. Nevirkovets[1], S.E. Shafranjuk[1], O. Chernyashevskyy[1], N. Masilamani[2], and J.B. Ketterson[1]

[1]*Department of Physics and Astronomy, Northwestern University, Evanston, IL 60208, USA*
E-mail: i-nevirkovets@northwestern.edu

[2]*Institute for Superconducting and Electronic Materials, University of Wollongong, Wollongong, NSW 2519, Australia*

Received May 30, 2013, revised August 6, 2013

We report on properties of Nb(/Ti)–carbon–(Ti/)Nb junctions fabricated on graphite flakes using e-beam lithography. The devices were characterized at temperatures above 1.8 K where a Josephson current was not observed, but the differential conductivity revealed features below the critical temperature of Nb, and overall metallic conductivity, in spite of a high-junctions resistance. Since the conductivity of graphite along the planes is essentially two-dimensional (2D), we use a theoretical model developed for metal/graphene junctions for interpretation of the results. The model involves two very different graphene "access" lengths. The shorter length characterizes ordinary tunneling between the three-dimensional Nb(/Ti) electrode and 2D graphene, while the second, much longer length, is associated with the Andreev reflections (AR) inside the junction and involves also "reflectionless" AR processes. The relevant transmission factors are small in the first case and much larger in the second, which explains the apparent contradiction of the observed behaviors.

PACS: 72.80.Vp Electronic transport in graphene;
74.45.+c Proximity effects; Andreev reflection; SN and SNS junctions;
74.50.+r Tunneling phenomena; Josephson effects;
74.78.Na Mesoscopic and nanoscale systems.

Keywords: carbon, graphene, superconductivity, tunnel junctions, Josephson effect, Andreev reflection.

1. Introduction

Graphene (G) is attractive as a barrier material for Josephson junctions due to high carrier mobility and unsurpassed flexibility in controlling its properties using various methods. In addition, such junctions offer an opportunity for physicists to study "relativistic" superconductivity [1] and unusual proximity effects [2]. Studying these effects and making useful devices is hampered, however, by the quality of the contacts between the G and metal banks [3–6]. Due to the difference in the work functions between the G and metals, Schottky-type barrier may be formed at the interface, thereby significantly changing the transport properties of the metal/G devices.

In attempt to study Nb/G Josephson junctions, we tested transport properties of Nb(/Ti)–carbon(C)–(Ti/)Nb junctions fabricated on exfoliated graphite flakes. Characteristics of the junctions are strongly dependent on the interface properties. In spite of a high junction resistance, presumably associated with the formation of potential barriers at the Nb(/Ti)–C interfaces, the junctions display an overall metallic conductivity. A theoretical model is proposed to explain this behavior.

2. Experiment

A total four devices were fabricated and tested. Graphite flakes were deposited onto oxidized Si substrates by mechanical exfoliation of highly-oriented pyrolytic graphite (HOPG). Using e-beam lithography, a PMMA mask was patterned on the graphite flakes. Then 2 nm of Ti was deposited, followed by 40 nm of Nb, to form devices G1 and G3; in devices G2 and G4, 40 nm thick Nb film was deposited directly onto the flakes. Prior to deposition of the Ti and Nb layers, 4 nm of the surface layer were removed from device G1 (made on thicker flake) by ion milling; no ion milling was used for devices G2 to G4 (which involve thinner flakes). The thickness of the flakes was measured using AFM. The device parameters are summarized in the Table 1. Figure 1(a) shows an SEM image of a typical device structure; Fig. 1(b) shows a schematic of the *I–V* curve measurement.

In order to record *I–V* curves, dc current from a battery-powered, computer-controlled power source was fed into the junction in steps of about 0.06 μA; the voltage across the junction was amplified and acquired by the computer using a National Instruments analog-to-digital converter.

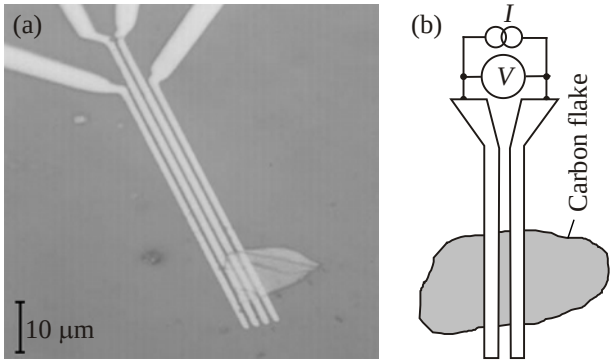

Fig. 1. SEM image of the device G1 made on 148 nm thick carbon flake (a) and schematic of the *I–V* curve measurement (b).

Table 1. Summary of the device parameters

Device number	Material of leads (in parentheses thickness in nm)	Spacing between the leads, nm	Flake thickness, nm	Device resistance at 5 K and 5 mV, Ω
G1	Ti(2)/Nb(40)	430	148	224
G2	Nb(40)	640	19	—
G3	Ti(2)/Nb(40)	440	9	369
G4	Nb(40)	170	8	600

Devices measurements were carried out in a Quantum Design PPMS cryostat at temperatures down to 1.8 K using a two-probe method. Due to the latter, the measured resistance (see Table 1) contains a 25 Ω contribution from the wires. Measurable characteristics were obtained for devices G1, G3, and G4; the resistance of the device G2 was too high to be measured with our technique.

The measured characteristics of the different devices were similar and displayed a nonlinearity of the *I–V* curve which was most pronounced for device G1. The *I–V* curves of this latter device, taken at various temperatures, are shown in Fig. 2(a). The junction resistance increases significantly with increasing temperature starting from about 7.0 K, indicating the beginning of transition of the Nb film into a resistive state (the critical temperature, T_c, is reduced for a 40 nm-thick Nb film as compared with usual $T_c \approx 9.0$ K for our thicker films).

At the temperatures of the experiment, a Josephson current was not observed in the *I–V* curves. In order to see if the *I–V* curves have nonlinearities, we differentiated them numerically to obtain *dV/dI* vs. *V* dependences. The most pronounced features were observed for sample G1 (see Fig. 2(b)). Numerical differentiation typically results in "noisy" curves. Better results can be obtained using ac modulation, a "physical differentiation" technique; however, in these preliminary experiments, we used the available digitized data, which already showed interesting properties. Specifically, we found that the differential resistance shows structure associated with the superconducting transition in Nb, and an overall metallic-like conductivity (initial portion is concave up), in spite of a high junction resistance presumably associated with the formation of potential barriers at the Nb/Ti–C interfaces. In order to better reveal the features in the noisy *dV/dI* vs. *V* dependences, we smoothed the curves using an adjacent averaging algorithm available from commercial software. As a result of averaging we obtained two traces (black curves) corresponding to "forward" and "backward" current ramping for the dependences taken at specific temperatures. Reproducibility of these traces, especially at the lowest temperatures, and the symmetry of the positions with respect to zero voltage (designated by arrows) argue that the observed nonlinearities are associated with the physical properties of the system and are not spurious. In samples G3 and G4 the nonlinearities were weaker, and the resistance of the junctions was higher, as shown in Table 1. Below we consider properties of the sample G1 in a more detail.

The dimensions of our sample as determined by AFM (Fig. 1(a)) are: Nb/Ti lead spacing, L = 430 nm; junction width, $W \approx 10$ μm; and flake thickness is 148 nm.

Given this thickness, the electric properties of the flake should be regarded as those of the graphite. Then, assum-

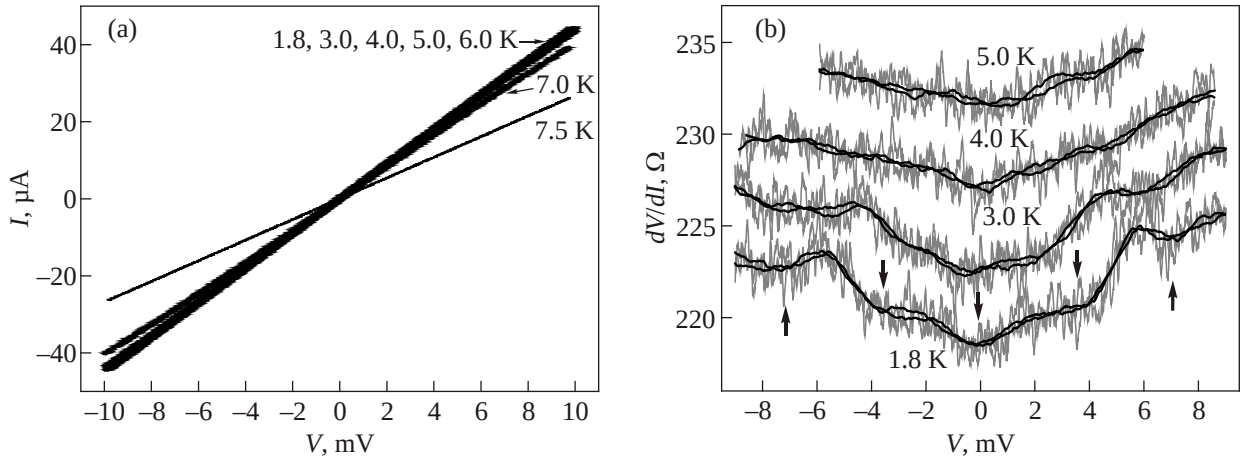

Fig. 2. I–V curves of Nb/Ti–C–Ti/Nb device (G1) at various temperatures from 1.8 to 7.5 K (a). Numerical derivatives, *dV*/*dI* (*V*), for the *I–V* curves measured at different temperatures *T*, K (thin grey lines). Curves for 3.0, 4.0, and 5.0 K are arbitrarily shifted in vertical direction for clarity. Thick black lines are averaged curves (see text for details) (b).

ing that the resistivity of graphite is about $9\cdot10^{-6}$ Ω·m, and taking into account its temperature dependence [7], we estimate that the resistance of our junction should be about 6 Ω; in fact, it is 224 Ω at low temperatures. Excluding the contribution of 25 Ω from the wires and 6 Ω from the graphite flake, we obtain a resistance of 193 Ω, which is probably originating from the interfaces between the Ti/Nb and the graphite flake.

Assuming that the two interfaces are identical, with an average area of A = 1 μm ×10 μm, we obtain the specific tunneling resistance ($R\times A$) of the interface to be of the order of 10^{-5} Ω·cm^2, indicating a rather strong barrier. It is known that such a barrier appears at the metal–G interface due to the different electron concentrations and work functions [6,8].

At lower temperatures, features are observed in the $dV/dI(V)$ dependences (marked by arrows in Fig. 2(b)). It is interesting to compare characteristic energies of these features with the Nb energy gap, Δ. Using the Bardeen–Cooper–Schrieffer (BCS) relation $2\Delta/k_BT_c = 3.52$ (where Δ is the superconducting energy gap, k_B is the Boltzmann constant, $k_B = 8.62\cdot10^{-5}$ eV/K), with $T_c \approx 7$ K as deduced above, we obtain an estimated maximum value $\Delta \approx 1$ meV. Because the device consists of two Nb/Ti–C junctions connected in series, one may expect manifestation of the gap-sum feature at about 2 mV; however, we observe a conductance peak within a voltage range of about ±1 mV (see curves for 1.8 K), and the conductivity anomalies at higher voltages (~4 and 7 mV). The first feature (conductance peak around zero voltage) may be indirectly related to the gap but rather to a contribution of the "reflectionless" Andreev reflection (AR) process (see our theoretical model below).

The features at about 4 and 7 mV (Fig. 2(b)) are unusual. A similar anomaly (as well as metallic junction type) was observed by Choi *et al*. for devices reported to be made from monolayer graphene [9]. The peaks at $V > 2\Delta/e$ can appear if the energy gap is induced in C, as explained in the next section. Further investigation is required to establish the nature of these features.

For this study, most important is the fact that the device conductance has a maximum at zero voltage (i.e., it is of metallic-type). Metallic type of conductivity takes place in junctions with high-conductive channels. Also, the conductance may continuously increase with voltage if the barrier is not rectangular but its width decreases with energy; it is suggested that the metal–G interface barrier has essentially a triangular shape [6,9]. The barrier is probably also asymmetric, as follows from the asymmetry of the $dV/dI(V)$ dependences with respect to zero voltage (cf. Fig. 2(b)). However, if a nonrectangular barrier is the only reason for the increase in the conductance, then it should not have an inflection point, as indicated here and in [9–11]. Therefore, we have to look for another mechanism for such behavior.

First, we analyze the junction resistance in a more detail. In general, there are three contributions to the junction resistance: (i) the Schottky barrier resistance due to difference of the work functions; (ii) a contribution due to a change in the number of channels for quantum tunneling from three-dimensional (3D) metallic electrode into the essentially two-dimensional (2D) graphite flake; and (iii) the resistance of the flake itself (estimated to be 6 Ω for the device G1); and (iv) a finite resistance originating from the mismatch of electronic properties between the two regions — the C just below the metal (G′), where electronic structure is modified due to the contact with the metal, and the open C region (G″). A schematic cross-sectional view of the device structure is shown in Fig. 3.

One can separate the contributions (i) and (ii) to the interface resistance from the experimental data by analyzing the ratio of the excess zero-voltage conductance (measured at a very low temperature) to the normal state conductance. We estimate this ratio by comparing zero-voltage differential resistance values at 1.8 K (the lowest temperature accessible in this experiment) and 5.0 K. The choice of the curve for 5.0 K is dictated by the fact that, at higher temperatures, an increasing overall shift of the differential resistance curve appears, indicating that some regions of the Nb leads become resistive below an estimated T_c value of 7 K; this makes the curves for higher temperatures unsuitable for the estimation. Then from the results shown in Fig. 2(b) we obtain an excess resistance for the 5.0 K curve of 2.7 Ω, which implies that the excess zero-voltage conductance due to contribution (ii) above is about 1.4% of the interface conductance. For the qualitative consideration, most important is presence of an excess conductance (the true value should be even slightly larger), which we discuss below.

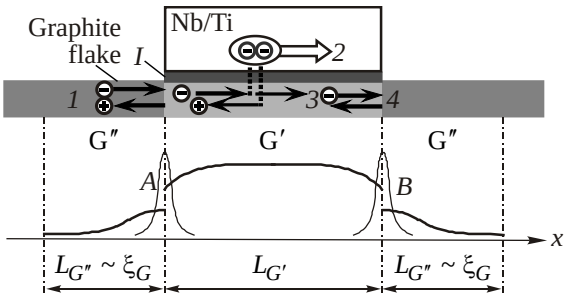

Fig. 3. Various processes involved in the electric transport in a Nb/Ti–C junction: in process *1*, an electron moving in 2D C flake from left can be either Andreev-reflected as a hole moving in opposite direction or normally reflected (not shown) from the interface *A* between the regions G″ and G′; inside the area G′, it can be either Andreev-reflected at the Nb/Ti–C interface I creating the Cooper pair in Nb (process *2*), or continue moving in the graphite sheet ballistically (process *3*). If the electron energy E is low ($E << U_0$), the electron bounces many times back and forth between the two barriers at $x = x_A$ and $x = x_B$ (process *4*) before it is either Andreev-reflected from the Nb/Ti–C interface or it escapes the contact region into the open C sections G″.

3. Theoretical model

A theoretical model proposed here is based on single-layer graphene that is a 2D material. The junction region in our devices contains many carbon layers; i.e., it is a graphite flake rather than graphene (although in the literature even multilayered carbon samples have been often referred to as graphene). However, the epitaxial graphite is highly anisotropic material with the conductivity along the crystal planes being hundreds of times larger than across the planes [12]. For this reason, we believe such a model can qualitatively explain transport properties of our system, specifically, the large value for the junction resistance (R_0 = 193 Ω in device G1) coexisting with the metallic-like shape of the *dV/dI(V)* curves at $T < T_{c,\mathrm{Nb}}$ as seen in Fig. 2(b).

On one hand, the overall high value of *dV/dI(V)* indicates that a low-transparency barrier is formed at the metal/carbon interface. On the other hand, the metallic-like shape of *dV/dI(V)* implies that the electric transport involves AR process that usually occurs at high-transparency interfaces. These two apparently contradictory facts can be reconciled within a model in which the metal/2D C contact is simulated by double-barrier S–I–G′–I–G″ junctions connected in series. The model is based on the modified BTK theory [13]. We shall show that the model qualitatively explains the experimental data taking into account the nanodevice geometry and the assumed interface structure. More technical details of the model are provided in the Appendix.

An important distinction between the junction considered within the BTK model [13] and our device is the change of electron state dimensionality 3D → 2D in the tunneling process between the Nb/Ti electrode (S electrode) and the C in the latter case. The number of quantum channels in 2D C is finite, which limits the tunneling probability from Nb/Ti into C.

Another difference between the BTK model and our geometries stems from a specific electron momentum conservation in our case. On one hand, only the electrons with momentum $p_\perp$ perpendicular to the interface contribute to the conventional tunneling (CT) between the Nb/Ti (S-electrode) and 2D carbon. On the other hand, only the electrons whose momentum $p_\parallel$ is parallel to the interface actually contribute to the AR process. This is due to the fact that the AR occurs on a much longer scale, of the order of the coherence length in 2D C ξ_G, rather than the regular tunneling across the C layers which occurs on a scale of order the lattice constant a [14]. Yet another difference between the model of Ref. 13 and our model is that, in the 1D geometry [13], an electron incoming from the N electrode reverses its momentum ($p_x \to -p_x$) after being normally reflected from the S/N interface barrier. For finite interface barrier strength $Z \neq 0$ this causes suppression of the electric current at voltages $|V| < \Delta_S / e$. In our geometry this does not happen since during the reflection at the S-I-G′ interface the x-component of the electron momentum is not reversed, $p_x \to p_x$.

Our model involves two very different characteristic scales — an "access" length [15], L_T, and the coherence length in 2D C, ξ_G, which are related as $L_T << \xi_G$. The short length $L_T \approx a$ characterizes CT of electrons between the 3D Ti/Nb electrode and 2D carbon perpendicular to the Nb/Ti–C interface ($p_\perp \neq 0$). The much longer ξ_G is related to AR at the 3D/2D Ti/Nb–C interface which occurs in parallel with the Nb/Ti–C interface ($p_\parallel \neq 0$). This is shown schematically in Fig. 3 as process *2*. Additionally there is another AR at the transitional G′/G″-region between the C section under the metal contact G′ (highlighted by lighter color in Fig. 3) and the C outside the contact region G″. We assume that the G′/G″ interfaces are characterized by potential barriers A and B shown in lower panel of Fig. 3 and located at $x = x_{A,B}$. The superconducting order parameter, Δ_G, induced due to the proximity effect, is finite not only in G′, but also in the uncovered C section G″, and spreads outside the contact area on the coherence length scale ξ_G. Thus the main contribution to the junction resistance comes from the CT through the Nb/Ti–G′ and G′/G″ interfaces.

The CT, acting during the first stage, actually restricts the AR to just a small fraction of electrons coming from Nb to C. The next stage is dominated by AR which takes place on a much longer spatial scale ξ_G. This AR process involves only the electrons whose momentum is parallel to the barrier component, i.e., $p_\parallel \neq 0$. In the latter case, since the contact length $L_c = L_{G'} + 2L_{G''}$ (see Fig. 3) is $L_c >> a$, the electrons spend much longer time L_c/v_F near the barrier before being Andreev-reflected (here v_F is the Fermi velocity in C). Because $L_c/v_F >> \tau_T$ (where τ_T is the CT time through the Nb/Ti–G′ barrier), the prolonged stay of electrons near the Nb/Ti–G′ barrier strongly increases probability of the AR T_2 as compared to the CT probability T_1 for electrons with $p_\parallel \neq 0$. Another important contribution comes from the "reflectionless" AR which happens when an electron spends sufficient time in vicinity of the N/S interface. The corresponding dwell time, τ_d, should much exceed the duration of an individual AR process, τ_{AR}, which is the case for an electron residing in the region G′. Furthermore, the τ_d is energy dependent. In our theoretical model we assume that the prolonged dwell time in the region G′ is caused by multiple reflections of electrons back and forth from the barriers A and B (see Fig. 3). In this model, the energy dependence of the τ_d naturally originates from the energy dependence of transparencies of the barriers A and B. At low energies, $E \sim 0$, the barriers are thicker and thus less transparent, which corresponds to a longer dwell time $\tau_d >> \tau_{AR}$. An electron tends to bounce several times between the barriers A and B before leaving the region G′. The barriers are thinner and more transparent as the electron energy increases, which makes the dwell time shorter,

$\tau_d \sim \tau_{AR}$. For this reason, the probability of the "reflectionless" AR is higher at low energies, and a conductance peak appears around zero voltage. We believe the feature within the voltage interval of about ±1 mV (cf. Fig. 2(b)) is caused by this process. The peak width is determined by the energy dependence of the transparencies of the barriers *A* and *B* rather than by the Nb energy gap magnitude.

Summarizing, all the electrons with $p_\perp \neq 0$ contribute into CT although its probability could be small due to presence of a finite interface barrier. On the other hand, only a small fraction of electrons with $p_\parallel \neq 0$ contribute to AR from the Nb/Ti–G′ interface, although the AR process probability is high. The associated transmission factors are small in the first case and much larger in the second case, which explains the apparent contradiction of the observed behaviors. The calculations have been performed by solving the Dirac equation for G and using the *S*-matrix technique extended to include superconducting correlations [1,2].

Since the real device (cf. Fig. 1) has two metal-carbon contacts, each of them assumed to have the double barrier S–I–G′–I–G″ structure shown in Fig. 3, the device is modeled by two S–I–G′–I–G″ junctions connected in series. Here S stands for the superconducting metal, I is the interface barrier, G′ is the carbon under the contact, G″ is the open carbon. The computed differential resistance *dV/dI(V)* of such a double barrier S–I–G′–I–G″ junction is shown in Fig. 4 where we used the S–I–G′ subjunction transparency, $T_1 = 0.04$, and the G′–I–G″ subjunction transparency, $T_2 = 0.65$. One sees three pronounced features in the *dV/dI(V)* curve. The feature within the voltage range ±1 mV corresponds to reflectionless tunneling, as described above. More specifically, as an electron traverses the contact area enclosed between the two barriers at $x = x_A$ and $x = x_B$, it either can be Andreev-reflected with probability T_1 at the S–I–G′ interface, or it can be normally reflected (or transmitted) with probability R_2 (T_2) at the G′–I–G″ interface barrier. The number of reflections depends on the electron's energy since the transparency of the potential barriers at $x = x_A$ and $x = x_B$ is energy-dependent. At low energies, the electron can bounce back and forth several times which increases the AR probability considerably [11]. This results in a pronounced minimum in the *dV/dI*(*V*) curve in the vicinity of $V = 0$. The second feature at $V \sim 2(\Delta_{\rm Nb} + \Delta_{G'})/e$ is related to AR in the S–I–G′ subjunction. Here $\Delta_{G'}$ is the proximity energy gap induced in the layer adjacent to the metal. There are two such S–I–G′ subjunctions in the measurement circuit which yields the coefficient 2. The third feature at $V \sim 2(\Delta_{\rm Nb} + \Delta_{G'} + \Delta_{G''})/e$ corresponds to AR at the G′–I–G″ subjunction which is connected in series with the S–I–G′ subjunction. Similarly, since there are two G′–I–G″ subjunctions in the circuit, it also gives the factor 2. Note that the shape of the feature at $V \sim 2(\Delta_{\rm Nb} + \Delta_{G'})/e$ is different from the shape of another feature at $V \sim 2(\Delta_{\rm Nb} + \Delta_{G'} + \Delta_{G''})/e$. The difference comes from different geometry of the S–I–G′ and G′–I–G″ subjunctions. During the reflection in the S–I–G′ junction, the *x*-component of the electron momentum is not reversed, $p_x \to p_x$, whereas it is reversed in the reflection process at the G′–I–G″ subjunction, resulting in $p_x \to -p_x$. The calculated data reveal an excess conductance at voltages $|V| \le 2(\Delta_{\rm Nb} + \Delta_{G'})/e$ for $1 > T_2 > 0.5$, in qualitative agreement with our experimental observation.

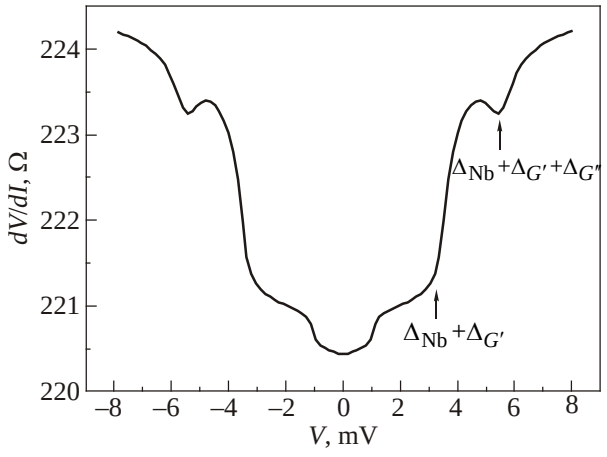

Fig. 4. Calculated differential resistance of the Nb/Ti–C–Ti/Nb junction. A broad minimum in the vicinity of zero bias is caused by the reflectionless tunneling inside the contact region ($x_A < x < x_B$). An even broader minimum at the voltages $|V| \le 2(\Delta_{\rm Nb} + \Delta_{G'})/e$ occurs due to the AR in the S–I–G′ subjunction (where $\Delta_{G'}$ is the proximity induced energy gap in the C under the metal). Additional tunneling-like feature occurs at $|V| \sim 2(\Delta_{\rm Nb} + \Delta_{G'} + \Delta_{G''})/e$ where $\Delta_{G''}$ is the proximity induced gap in the open carbon regions G″ right outside the contact area (cf. Fig. 3).

Similar excess conductance has been reported not only for superconductor–graphene–superconductor junctions [9–11], but also for the Nb/Pd–CNT–Pd/Nb junctions (where CNT stands for carbon nanotube) [16,17], implying that our model may be applicable for a broader class of systems than considered here.

4. Conclusion

Experimental data on Nb(/Ti)–C–(Ti/)Nb junctions reveal a strong barrier at the metal–C interfaces, which probably results in suppression of Josephson current in the devices down to 1.8 K. However, the device conductivity is metallic-type, which is not expected for the strong interface barriers. A theoretical model is presented which explains this apparent contradiction in terms of two tunneling processes: CT between the Nb(/Ti) electrode and 2D carbon, and the second process, associated with the AR which also involves "reflectionless" processes. The associated transmission factors are small in the first case and much larger in the second case, leading to a noticeable contribution of the AR to the conductivity.

It should be noted that interfacial phenomena between a superconductor and carbon (in the form of both graphite

and graphene) are not well studied, both experimentally and theoretically. Clearly more experimental work is needed to study this system.

The authors are thankful to Prof. S.X. Dou for his attention to this work. I.P. Nevirkovets acknowledges support provided by the Australian National Fabrication Facility (ANFF) through the Australian National Collaborative Research Infrastructure Strategy (NCRIS) during his work at the University of Wollongong.

Appendix

Below we provide details on the theoretical model that has been used to interpret the data from this experiment. We assume that the overall electron transmission trajectory through the S–I–C–I–S junction is represented by a broken line since CT takes place in the *z*-direction while AR involves the *x*-direction. Note that the broken-line trajectory (cf. Fig. 5(a)) differs from the straight-line trajectory considered in the Ref. 13. The *major distinction* between our geometry and that considered in the original BTK model [13] is that there is no conventional reflection at the superconductor — 2D carbon (S–I–C) interface in our geometry: when an electron inside the C sheet approaches the vicinity of the S–I–C contact, it either penetrates through the S–I–C interface with a certain probability T_1 or it continues moving ahead inside the same carbon sheet, thereby directly transmitted the S–I–C contact area without any reflection. Only those electrons penetrating the S electrode contribute to the AR process whereas the directly transmitted electrons do not. Note, the CT and the AR processes occur on different scales (~a for the former and ~ξ_G for the latter). Because the electron trajectory in our case is not a straight line, the two different scales serve to spatially separate the microscopic tunneling from the AR.

We describe the electron transport properties of the S–I–G′–I–G″ junction (cf. Fig. 3) within the scattering matrix approach by assuming that the carbon sheet is monolayer G and that the major contribution comes from the vicinity of the K(K')-point. The incoming $\breve{\Psi}_i$ and outgoing $\breve{\Psi}_o$ envelope electron wave functions are connected by the S-matrix as $\breve{\Psi}_o = \breve{S}\breve{\Psi}_i$ [16]. Following Refs. 1, 2, AR in G must also account for the electron/hole chirality. This causes a more complex structure of electron and hole states in graphene, and also introduces new features into the AR at the superconducting metal/G interface as compared to conventional materials. In the G junctions, one may observe not only the conventional Andreev retro-reflection, which takes place inside the same (conduction) band, but also a specular AR which occurs as the result of an interband processes. The $\breve{\Psi}_{o(i)}$ states are represented by vectors

$$\breve{\Psi}_{o(i)} = \begin{pmatrix} \hat{\psi}^o_L \\ \hat{\psi}^o_R \end{pmatrix}, \; \hat{\psi}^{o(i)}_{L(R)} = \begin{pmatrix} u^{o(i)}_{L(R)} \\ v^{o(i)}_{L(R)} \end{pmatrix}. \qquad (A.1)$$

Here $\hat{\psi}^{o(i)}_{L(R)}$ are the Nambu spinors composed of the electron ($u^{o(i)}_{L(R)}$) and of its time-reversed hole ($v^{o(i)}_{L(R)}$) states. The wave functions $u^{o(i)}_{L(R)}$ and $v^{o(i)}_{L(R)}$ describe incoming and outgoing electrons and holes from the left (L) and right (R) of the scatterer, which together constitute the S–I–G–I–S junction. As compared to spinless electron states in conventional conductors, the electrons and holes in G are characterized by additional quantum numbers which are the two 1/2-pseudospins. Therefore an electron state $u^{o(i)}_{L(R)}$ is represented by a *four-dimensional* vector $u = (\phi_A, \phi_B, -\phi'_B, \phi'_A)$ where the indices A and B denote two different G sublattices while the prime indicates the K′ valley. The corresponding hole state $v^{o(i)}_{L(R)}$ is represented as $v = Tu = (\phi^*_A, \phi^*_B, -\phi^*_B, \phi^*_A)$, where T is the time reversal operator [1,2]. The Cooper coupling between u and v is determined from the Dirac–Bogoliubov–de Gennes equation [1]:

$$\begin{pmatrix} H - E_F & \Delta(\sigma_0 \otimes \tau_0) \\ \Delta^*(\sigma_0 \otimes \tau_0) & -(H - E_F) \end{pmatrix} \begin{pmatrix} u \\ v \end{pmatrix} = \varepsilon \begin{pmatrix} u \\ v \end{pmatrix}, \qquad (A.2)$$

where $H = v(\mathbf{p}\cdot\boldsymbol{\sigma}) \otimes \tau_0 + U(r)\sigma_0 \otimes \tau_0$, Δ is the superconducting pair potential which couples u and its time-reversed state, v. The S-matrix has the following structure:

$$\breve{S} = \begin{pmatrix} \hat{r} & \hat{t} \\ \hat{t}^\dagger & \hat{r} \end{pmatrix}, \; \hat{r} = \begin{pmatrix} r & r^*_A \\ r_A & r^* \end{pmatrix}, \; \hat{t} = \begin{pmatrix} t & t^*_A \\ t_A & t^* \end{pmatrix}; \qquad (A.3)$$

here one sees that in addition to the diagonal elements, which correspond to the conventional reflection (r) and transmission (t) amplitudes, there are also nondiagonal elements r^A and t^A which describe the AR processes. The r and t amplitudes are 4×4 matrices since they also account for the 1/2-psuedospin flips.

The transmission through the S–I–G–I–S junction can be represented by two S-matrices S_T and S_A

$$S_{\text{tot}} = S_T \tilde{\otimes} S_A, \qquad (A.4)$$

where S_T corresponds to pure tunneling on a "short" scale (~a) perpendicular to the S/G-interface, while S_A describes a pure AR happening on a "long" scale ~ξ_G inside S. The composition rules for the reflection r, r' and transmission t, t' amplitudes are:

$$\begin{aligned} t_{\text{tot}} &= t_2(I - r'_1 r_2)^{-1} t_1; \\ r_{\text{tot}} &= r_1 + t'_1 r_2 (I - r'_1 r_2)^{-1} t_1; \\ t'_{\text{tot}} &= t'_1 [I + r_2 (I - r'_1 r_2)^{-1} r'_1] t'_2; \\ r'_{\text{tot}} &= r'_2 + t_2 (I - r'_1 r_2)^{-1} r'_1 t'_2. \end{aligned} \qquad (A.5)$$

Every partial S-matrix S_i (here $i = T, A$) connects the incoming and outgoing states for the ith scatterer. The reflection and transmission amplitudes in Eqs. (A.5) are themselves 8×8 matrices (because for each u-v coupling there are two ± orientations of the two 1/2-pseudospins).

For definiteness we also assume that the electron transport is coherent, i.e., the CT and AR are phase-correlated. Then we combine the successive sections coherently. If the scattering is incoherent we should not use the scattering amplitudes but rather the scattering probabilities [16]. Our experimental data do not indicate the presence of specular AR [1]. Therefore, for the sake of simplicity, we only consider conventional AR (an incident electron is converted into a Cooper pair and a retro-reflected hole). In addition, we adopt the BTK approximation [13] that the interface barrier shape is described by a Dirac δ-function. Under these assumptions, the *S*-matrix for the pure tunneling amplitudes through the interface barrier is approximated by

$$\breve{S}_T = \begin{pmatrix} \hat{r}_1 & \hat{t}_1 \\ \hat{t}_1^{\dagger} & \hat{r}_1' \end{pmatrix}, \ \hat{r} = \begin{pmatrix} r_1 & 0 \\ 0 & r_1' \end{pmatrix}, \ \hat{t} = \begin{pmatrix} t_1 & 0 \\ 0 & t_1' \end{pmatrix}, \quad \text{(A.6)}$$

where we neglect the AR processes. On the other hand, the *S*-matrix of a pure AR is

$$\breve{S}_A = \begin{pmatrix} \hat{r}_2 & \hat{t}_2 \\ \hat{t}_2^{\dagger} & \hat{r}_2 \end{pmatrix}, \ \hat{r}_2 = \begin{pmatrix} 0 & r_A^* \\ r_A & 0 \end{pmatrix}, \ \hat{t}_2 = \begin{pmatrix} t_2 & 0 \\ 0 & t_2' \end{pmatrix}, \quad \text{(A.7)}$$

where we neglect the conventional reflection and tunneling amplitudes. The reflection and transmission amplitudes r_1 (r_1'), $t_1(t_1')$, and $t_2(t_2')$ entering Eqs. (A.6) and (A.7) connect the incoming and outgoing states $u = (\phi_A, \phi_B, -\phi_B', \phi_A')$ and $v = (\phi_A'^*, \phi_B'^*, -\phi_B^*, \phi_A^*)$; therefore, they are matrices 4×4. The CT preserves the particle's chirality, thus one sets $t_i = t\cdot\hat{1}$ where $\hat{1}$ is the 4×4 unit matrix. The AR preserves the time invariance and couples the electron state u and its time-reversed hole state v which has an opposite momentum (i.e., the corresponding electron and hole are located at the K and K' points). Thus one sets $r_A^i = r_A T = -r_A(\tau_2 \otimes \sigma_2)C$ where T and C are the time reversal and the complex conjugation operators, respectively. The composite AR amplitude of an S–N–I–N junction is then obtained as

$$r_A = \frac{e^{i\varphi} t_1^2 r_A^*}{1 - r_1^2 |r_A|^2}, \quad \text{(A.8)}$$

while the composite conventional reflection amplitude is

$$r = r_1 \frac{1 + (t_1^2 - r_1^2)|r_A|^2}{1 - r_1^2 |r_A|^2}; \quad \text{(A.9)}$$

the composite CT amplitude is

$$t = \frac{t_1 t_2}{1 - r_1^2 |r_A|^2}. \quad \text{(A.10)}$$

Our experimental data can be understood if we take into account conventional AR as in the BTK model [13]. Then we use:

$$r_i = Z_i \frac{(2i - Z_i)}{D_A^{(i)}}(u_{0,i}^2 - v_{0,i}^2), \quad r_A^{(i)} = 4\frac{v_{0,i}\, u_{0,i}\, e^{i\varphi}}{D_A^{(i)}},$$
$$t_i = 2\frac{u_{0,i}\,(2 + iZ_i)}{D_A^{(i)}} e^{i\frac{\varphi}{2}}, \quad t_A^{(i)} = -\frac{2iv_0^{(i)} Z_i}{D_A^{(i)}} e^{i\frac{\varphi}{2}}. \quad \text{(A.11)}$$

Here $i = 1, 2$; Z_i is the interface barrier strength,

$$D_A^{(i)} = 4(u_0^{(i)})^2 + Z_i^2[(u_0^{(i)})^2 - (v_0^{(i)})^2],$$
$$u_0 = \sqrt{1 + \xi_\varepsilon/\varepsilon}/\sqrt{2}, \ v_0 = \sqrt{1 - \xi_\varepsilon/\varepsilon}/\sqrt{2}.$$

One also obtains

$$R_1 = |r_1|^2 = Z_1^2/(Z_1^2 + 4), \ T_1 = |t_1|^2 = 1 - R_1 = 1/[(Z_1/2)^2 + 1],$$

which for $T_1 = 10^{-6}$ gives $Z_1 = 2\cdot10^2$. The S–I–G interface barrier strength Z_1 is expressed via the interface barrier transparency T_1 as $Z_1 = 2\sqrt{(1 - T_1)/T_1}$. As an illustrative example, we first assume that no superconducting proximity gap is induced in C. We then represent the S–I–C–I–S junction as a combination of two S–N–I–N and N–I–N–S block junctions. In the simplest approximation $Z_2 = 0$ (i.e., there are no barriers at the S/N and N/S interfaces). Then, in the one-dimensional BTK model, one gets $r_1 = Z_1(2i - Z_1)/(4 + Z_1^2)$. On the other hand, in our broken-line model, we use $r_1 = 0$. The other parameters are common for the both cases, $t_1 = (1 + iZ_1/2)/(1 + Z_1^2/4)$, $t_A^{(1)} = 0$, $t_2 = 1/u_0$, $r_A^{(2)} = (v_0/u_0)$, $r_2 = 0$, and $t_A^{(2)} = 0$. We also consider an additional contribution from multiple AR processes occurring when an electron bounces back and forth inside the contact region G′. Such multiple processes are illustrated in Fig. 3. The multiple AR scenario takes place as follows. An electron *e* enters the contact region G′ from the uncovered C section G″. Since there are two potential barriers separating the G′ and G″ regions [11,18], after entering G′, the electron is Andreev-reflected many times inside G′ before it exits into G″ region. The multiple AR processes are described by higher-order products

$$\breve{S}_{TA}^{(2)} = \left(\breve{S}_T \,\tilde{\otimes}\, \breve{S}_A\right)\tilde{\otimes}\, \breve{S}_A$$
$$\breve{S}_{TA}^{(N+1)} = \breve{S}_{TA}^{(N)} \,\tilde{\otimes}\, \breve{S}_A \quad \text{(A.12)}$$

etc., where 4x4 matrices S_T and S_A are given by Eqs. (A.6) and (A.7).

We will assume that the barrier transparency is energy-dependent with the barrier shapes modeled as $U(x) = U_0 \exp(-(x - x_A)^2/b^2)$, where b is the geometrical barrier width. Parameters x_A and b of the interface barrier separating the G′ and G″ regions are obtained from fitting the experimental *I–V* curve. Then, if an electron leaving the carbon G″ region arrives in G′ region, its further propagation is as follows. (i) It is Andreev reflected at the Nb/Ti–C interface, creating a Cooper pair in the Nb and a hole moving back into barrier *A* located at $x = x_A$ (cf. Fig. 3). Consequently, the hole is reflected from the barrier *A* or tunnels through it.

Substituting the amplitudes t_i and r_i into Eqs. (A.10)–(A.12), and also into the BTK formula for the electric current yields

$$I = \frac{2e^2}{h}\int dE\, M(E)\left(|t(E)|^2 + |r_A(E)|^2\right)(f_F - f_{F-eV}), \quad \text{(A.13)}$$

where $M(E)$ is the number of modes in the carbon, f_F is the Fermi distribution function, V is the bias voltage. The conductance computed from the above Eq. (A.12) is represented in Figs. 5(b),(c). In Fig. 5(b), we plot the conductance of the S–N–I–N block junction assuming that there is no conventional reflection at the N–I–N interface (i.e., we set $r_1 = 0$ according to our broken-line trajectory model). From Fig. 5(b), one can infer that the conductance vs. voltage dependence follows the shape of the barrierless AR, while its amplitude is strongly reduced due to the low-tunneling amplitude, $t_1^2 << 1$, through the interface barrier I. For comparison, Fig. 5(c) represents results for the conventional BTK model that assumes the electron trajectory is a straight line and the reflection coefficient is finite and defined as $r_1 = Z_1(2i - Z_1)/(4 + Z_1^2) \neq 0$.

A more realistic correspondence with our experimental data can be achieved if we assume that a finite superconducting energy gap is induced in carbon as a result of the proximity effect. We then have an S–S′–I–N block junction rather than an S–N–I–N junction. Qualitative agreement with the experimental data shown in Fig. 2(b) can be obtained if we assume that the energy gap Δ' induced by the superconducting metal electrode in the carbon region G′ (i.e., S′) is only slightly smaller than Δ in S. The S–S′–I–N–I–S′–S junction is composed of two S–S'–I–N and N–I–S′–S block junctions (cf. Fig. 5(a)); its calculated differential resistance *dV/dI* vs. voltage *V* is shown in Fig. 4. The calculation shows that there is a visible suppression of the resistance at voltages $-(\Delta_{Nb} + \Delta_G)/e < V < (\Delta_{Nb} + \Delta_G)/e$ occurring when the AR probability $1 > T_2 > 0.5$. In our experiment, the excess Andreev conductance (which corresponds to the suppressed differential resistance) occurs in the bias voltage interval corresponding to four S–I–S′ junctions connected in series. The two junctions originate immediately from the Nb/Ti–C 3D/2D interfaces, whereas two additional S′–I–S″ junctions are formed inside the carbon layer between the region underneath of metal (G′) and outside adjacent region (G″) as shown in the lower panel of Fig. 3. The four junctions connected in series thus provide the bias voltage interval $-4(\Delta_{Nb} + \Delta_G)/e < V < 4(\Delta_{Nb} + \Delta_G)/e$ (where $(\Delta_{Nb} + \Delta_G)/e \approx 1.9$ mV) for the excess Andreev conductance (suppressed resistance). Similar phenomena have been reported recently for the Nb/Pd/CNT/Pd/Nb junctions [16,17].

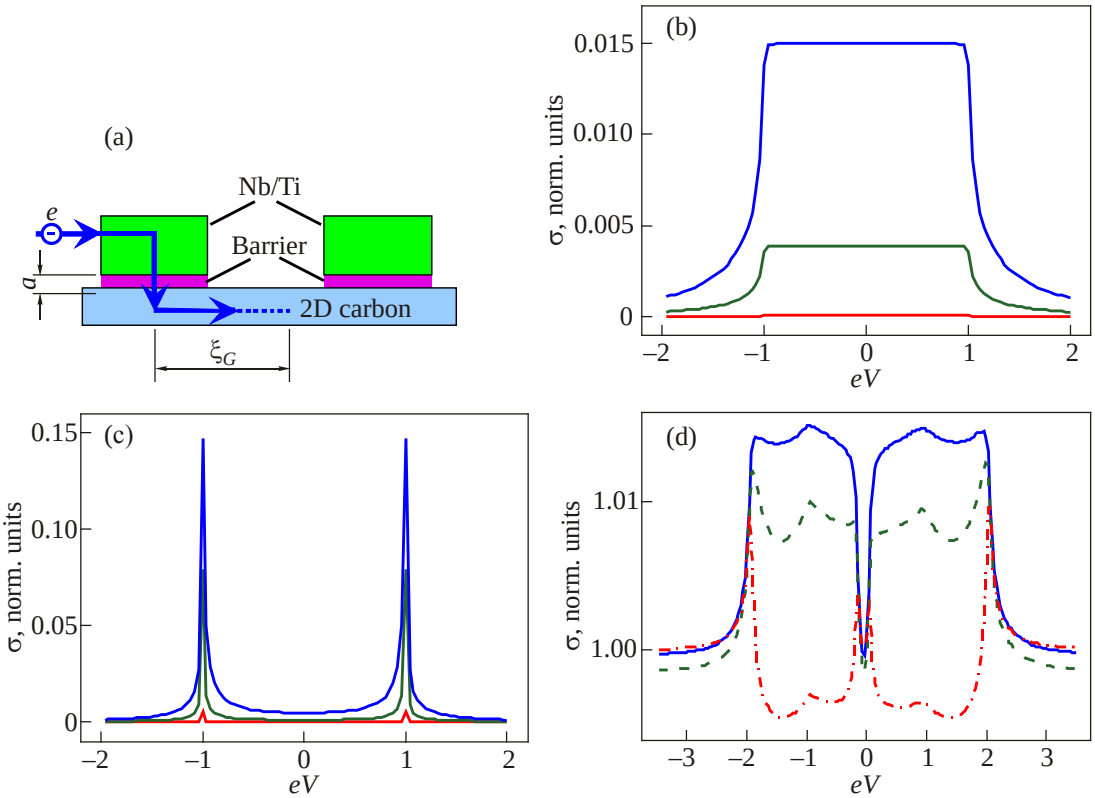

Fig. 5. (Color online) The Nb/Ti–C–Nb/Ti junction which is composed of two Nb/Ti–C block contacts. Each of the Nb/Ti–C contacts is represented in our model by the double barrier S–I–G′–I–G″ junction (cf. Fig. 3 in the main text) (a). The normalized "reflectionless" conductance σ(*V*) of the S–N–I–N junction computed within the BTK model with the broken line trajectory ($r_1 = 0$). The energy gap is $\Delta = 1 + i \cdot 0.002$, transmission coefficient through the barrier I is $t_1 = 0.3$, 0.8 and 0.95 (b). The same characteristic as before but for the straight line electron trajectory when $r_1 = Z_1(2i - Z_1)/(4 + Z_1^2)$ (c). AR in the asymmetric S–I–S′ junction where S and S′ are superconducting electrodes characterized by different energy gaps $\Delta' = 0.8\Delta$ (d).

1. C.W.J. Beenakker, *Rev. Mod. Phys.* **80**, 1337 (2008).
2. C.W.J. Beenakker, *Phys. Rev. Lett.* **97**, 067007 (2006).
3. G. Liang, N. Neophytou, M.S. Lundstrom, and D.E. Nikonov, *Nano Lett*. **8**, 1819 (2008).
4. T. Mueller, F. Xia, M. Freitag, J. Tsang, and Ph. Avouris, *Phys. Rev. B* **79**, 245430 (2009).
5. P.A. Khomyakov, G. Giovannetti, P.C. Rusu, G. Brocks, J. van den Brink, and P.J. Kelly, *Phys. Rev. B* **79**, 195425 (2009).
6. Ph. Avouris, *Nano Lett*. **10**, 4285 (2010).
7. J.M. Skowronski, *Carbon* **26**, 613 (1988).
8. E.J.H. Lee, K. Balasubramanian, R.T. Wetz, M. Burghard, and K. Kern, *Nature Nanotech*. **3**, 486 (2008).
9. J.-H. Choi, H.-J. Lee, and Y.-J. Doh, *J. Korean Phys. Soc*. **57**, 149 (2010).
10. D. Jeong, J.-H. Choi, G.-H. Lee, S. Jo, Y.-J. Doh, and H.-J. Lee, *Phys. Rev. B* **83**, 094503 (2011).
11. M. Popinciuc, V.E. Calado, X.L. Liu, A.R. Akhmerov, T.M. Klapwijk, and L.M.K. Vandersypen, *Phys. Rev. B* **85**, 205404 (2012).
12. P.R. Wallace, *Phys. Rev.* **71**, 622 (1947).
13. G.E. Blonder, M. Tinkham, and T.M. Klapwijk, *Phys. Rev. B* **25**, 4515 (1982).
14. K. Sugihara, *Phys. Rev. B* **29**, 5872 (1984).
15. D. Kaufman, B. Dwir, A. Rudra, I. Utke, A. Palevski, and E. Kapon, *Physica E* **7**, 756 (2000).
16. J. Zhang, A. Tselev, Y. Yang, K. Hatton, P. Barbara, and S. Shafranjuk, *Phys. Rev. B* **74**, 155414 (2006).
17. A. Tselev, Y.Yang, J. Zhang, P. Barbara, and S.E. Shafranjuk, *Phys. Rev. B* **80**, 054504 (2009).
18. F. Xia, V. Perebeinos, Y. Lin, Y. Wu, and P. Avouris, *Nature Nanotechnol*. **6**, 179 (2011).